

Spatiotemporal patterns of temperature inversions and impacts on surface PM_{2.5} across China

Yonglin Fang¹, Hancheng Hu¹, Xiangdong Zheng², Jianping Guo³, Xingbing Zhao⁴, Fang Ma⁵, Hao Wu¹

¹Chengdu University of Information Technology, China Meteorological Administration Radar Meteorology Key Laboratory, Chengdu 610225, China

²Chinese Academy of Meteorological Sciences, Beijing 100081, China

³State Key Laboratory of Severe Weather Meteorological Science and Technology & Specialized Meteorological Support Technology Research Center, Chinese Academy of Meteorological Sciences, Beijing 100081, China

⁴Chengdu Institute of Plateau Meteorology, China Meteorological Administration, Chengdu 610072, China

⁵Yunnan Atmospheric Observation Technology Support Center, Kunming 650034, China

Correspondence: Hao Wu (wuhao@cuit.edu.cn)

Abstract. Temperature inversions (TIs) strongly regulate the accumulation and dispersion of air pollutants, yet their nationwide impacts on surface PM_{2.5} remain poorly quantified. Here we integrate high-resolution L-band radiosonde profiles with PM_{2.5} monitoring data from 2016–2021 to characterize the frequency, strength, thickness, and diurnal variability of TIs—including surface-based inversions (SBIs) and elevated inversions (EIs)—across mainland China. We show that TIs are pervasive, occurring on average 52% of days, with mean strength of 2.1 °C and thickness of 214 m, and are more common at 08:00 than 20:00. Distinct regional patterns emerge: SBIs dominate in northern China, whereas EIs prevail in eastern China. Overall, SBIs are 1.3 °C stronger than EIs. TIs intensify seasonal pollution, with 76% of PM_{2.5} episodes coinciding with inversion events. SBI strength correlates positively with PM_{2.5} concentrations nationwide, while EI parameters show negative associations in eastern and southern regions. These findings reveal the spatiotemporal dynamics of TIs, establish quantitative links to surface pollution, and highlight regionally divergent mechanisms, providing critical insight for air-quality forecasting and targeted emission control.

Keywords: Temperature inversion, PM_{2.5}, Air pollution, Radiosonde profiles.

1 Introduction

Fine particulate matter (PM_{2.5}, aerodynamic diameter $\leq 2.5 \mu\text{m}$) is a dominant component of atmospheric aerosols and a key indicator and a primary pollutant of air pollution in China (Liang et al., [2021](#); Luo et al., [2024](#); Yan et al., [2023](#); Zang et al., [2021](#)). Over the past two decades, recurrent severe haze episodes characterized by elevated PM_{2.5} levels have imposed substantial public health burdens, including respiratory, cardiovascular, and reproductive impairments, as well as increased cancer risk (Chan and Yao, [2008](#); Yan et al., [2021](#); Garcia et al., [2023](#); Rentschler and Leonova, [2023](#); Zuo et al., [2023](#); Chen et al., [2025](#)). In response, stringent emission control policies since 2013 have markedly improved air quality, with annual mean

31 PM_{2.5} concentrations declining from 68 $\mu\text{g m}^{-3}$ in 2013 to 29 $\mu\text{g m}^{-3}$ in 2022 (Meng et al., [2023](#); Peng et al., [2025](#); Zou et al.,
32 [2025](#)). Nevertheless, seasonal pollution episodes remain acute, particularly in the Beijing–Tianjin–Hebei (BTH) region, where
33 the 2022 annual mean still reached 44 $\mu\text{g m}^{-3}$ (Ministry of ecology and environment the people’s republic of China, [2022](#)),
34 exceeding the World Health Organization’s Stage-1 interim target of 35 $\mu\text{g m}^{-3}$ (WHO, [2021](#)). Growing evidence shows that
35 such extreme events are not solely determined by anthropogenic emissions but are strongly modulated by adverse
36 meteorological conditions, among which temperature inversion (TI) plays a pivotal role (Feng et al., [2020](#); Morawska et al.,
37 [2021](#); Deng et al., [2022](#); Shao et al., [2023](#); Sun et al., [2025](#)).

38 In meteorology, TI refers to the anomalous increase of temperature with altitude, most frequently observed in the lower
39 troposphere. TIs arise through multiple mechanisms, including nocturnal radiative cooling, warm-air advection, topographic
40 confinement, as well as under specific synoptic conditions such as stationary high-pressure systems (subsidence warming) and
41 frontal zones (Vihma et al., [2011](#); Kassomenos et al., [2014](#); Largeron and Staquet, [2016](#); Xu et al., [2019](#)). Surface-based
42 inversions (SBIs) typically form at night when radiative cooling produces a shallow, stable layer of cold air near the surface,
43 which usually dissipates after sunrise or under strong winds ($>20 \text{ km h}^{-1}$) (Czarnecka et al., 2019). In contrast, elevated
44 inversions (EIs) are often associated with synoptic-scale phenomena. Key driving mechanisms include synoptic-scale warm
45 advection, subsidence within high-pressure systems, and frontal overrunning (Huang et al., 2021; Palarz et al., 2018).

46 The presence of TI suppresses turbulent mixing, strengthens atmospheric stability, and traps pollutants near the surface
47 (Kahl, [1990](#); Zhong et al., [2018](#)). Within the boundary layer, this stable stratification creates a pronounced “capping effect”
48 that critically limits vertical pollutant dispersion (Stull, [1988](#)). The resulting suppression of atmospheric pollutant dispersion
49 and transport operates through three interconnected mechanisms. First, the inversion layer itself acts as a meteorological cap,
50 inhibiting vertical mixing and fostering rapid near-surface accumulation of aerosols (Zhong et al., [2017](#)). Second, synoptic
51 conditions conducive to inversion formation—particularly for surface-based inversions—are often accompanied by weak
52 horizontal winds, further restricting advective transport (Yang and Shao, [2021](#)). Third, the persistence of inversions, especially
53 under wintertime high-pressure systems, prolongs pollution episodes over multiple days, allowing progressive buildup of PM_{2.5}
54 and compounding air quality deterioration (Feng et al., [2020](#)). Collectively, these processes establish TIs as a pivotal
55 meteorological driver of severe pollution across diverse regions.

56 Extensive research over the past two decades has examined the characteristics of TIs and their interactions with air
57 pollution (Rendón et al., [2015](#); Wolf et al., [2014](#); Wu et al., [2014](#); Yin et al., [2021](#)). Early studies highlighted their synoptic
58 controls: Milionis and Davies ([1992](#)) identified upper-level inversions between 950–800 hPa over Hemsby, UK, primarily
59 associated with subsidence within anticyclonic systems. At a continental scale, Zhang et al. ([2011](#)) analyzed radiosonde data
60 from 50 U.S. stations and showed that lower-tropospheric inversions (LTIs) are widespread, with strong zonal wind shear
61 playing a key role in their formation. More recently, advanced remote sensing has enabled quantitative assessment of
62 inversion–aerosol interactions. For example, Liu et al. ([2022](#)) combined lidar and radiosonde measurements over the Southern

63 Great Plains to demonstrate that inversion intensity critically determines the aerosol-trapping capacity of the boundary layer.

64 Nonetheless, most existing studies remain limited to individual cities or specific regions. For example, Wallace et al.
65 (2009) showed that nocturnal inversions in Hamilton, Canada increased $PM_{2.5}$ concentrations by 54%, with mobile
66 observations further revealing the reinforcing role of local topography in inversion formation and pollutant buildup. In China,
67 Xu et al. (2019) reported that 93% of heavy pollution episodes in Beijing coincided with inversion conditions, while Feng et
68 al. (2020) found that winter inversions in the Sichuan Basin elevated $PM_{2.5}$ levels by 64.7% compared with non-inversion days.
69 Beyond China, Lagmiri and Dahech (2024) identified inversions as the dominant driver of particulate pollution in Cergy-
70 Pontoise, France, with nearly 80% of PM_{10} exceedances occurring under inversion conditions persisting 1–3 days in winter.
71 Structural analyses have also revealed multi-layer inversion systems: Li et al. (2012) described a four-tiered inversion structure
72 over central China, linking mid-tropospheric inversions to synoptic cold fronts and regional advection, while upper-level
73 inversions exhibited strong latitudinal dependence.

74 While these studies underscore the critical role of inversions in pollution accumulation, substantial knowledge gaps
75 remain regarding their nationwide patterns and interactions with $PM_{2.5}$ across China's diverse climatic and topographic settings.
76 The country's complex geography—spanning plains, basins, and plateaus—produces pronounced regional heterogeneity in
77 inversion mechanisms and vertical structures (Yang et al., 2025). For instance, the North China Plain is frequently subjected
78 to strong wintertime SBIs, whereas the Sichuan Basin is characterized by deep, persistent inversions confined by topography
79 (Guo et al., 2020; Huang et al., 2021; Xu et al., 2021). Such spatial variability drives region-specific impacts on $PM_{2.5}$
80 accumulation, underscoring the need for systematic, high-resolution observational analyses. Although Yang and Shao (2021)
81 documented a nationwide increase in inversion frequency over the past three decades using reanalysis products, the coarse
82 vertical resolution of datasets such as ERA5 (25 hPa layers) hampers accurate representation of inversion structure. Similarly,
83 radiosonde-based studies (Guo et al., 2020; Huang et al., 2021; Xu et al., 2021) have provided valuable regional insights but
84 fall short of offering a comprehensive national-scale assessment of boundary-layer inversions and their impacts on $PM_{2.5}$
85 pollution.

86 In this study, we employ high-vertical-resolution radiosonde observations (6–8 m) from 2016 to 2021 to accurately detect
87 inversion layers and their vertical structures, thereby overcoming the coarse limitations of reanalysis data. By integrating these
88 measurements with nationwide $PM_{2.5}$ monitoring records from the Ministry of Ecology and Environment, we systematically
89 characterize the spatiotemporal distribution of TIs across China, quantify the distinct impacts of SBI and EI on surface $PM_{2.5}$
90 concentrations, and establish dynamic relationships between inversion parameters and pollution levels. These findings provide
91 new mechanistic insight into inversion–pollution interactions and offer scientific support for region-specific air quality
92 forecasting and management.

93

94 2 Study area and Data

95 2.1 Study area

96 Our analysis covers mainland China, a region of vast spatial extent and pronounced physiographic complexity where
97 monsoonal and continental regimes interact to produce strong environmental heterogeneity. To capture this diversity, we
98 partition the domain (excluding Hong Kong, Macau, and Taiwan owing to data limitations) into seven regions based on
99 standard administrative divisions, integrated meteorological characteristics and major urban agglomerations (Fig. 1). The
100 Northeast (NE)—a traditional industrial base with cold, dry winters—features emissions dominated by coal-fired heating and
101 heavy industry. North China (NC), including the Beijing–Tianjin–Hebei megacity cluster, is characterized by dense population,
102 intensive industrial and vehicular activity, and frequent severe haze. The Northwest (NW) comprises plateaus, basins, and
103 deserts under a continental climate with strong insolation and large diurnal temperature ranges; dust and energy/chemical
104 sectors are major contributors. East China (EC) and South China (SC) lie in the East Asian monsoon zone and are among the
105 most economically active regions, influenced by industrial and traffic emissions and regional transport. Central China (CC),
106 located in the heart of the country, experiences a transitional monsoon climate between the northern subtropical and warm
107 temperate zones, characterized by a terrain dominated by plains and hills. Pollutants tend to accumulate in basins such as the
108 Jiangnan–Dongting Basin due to the region’s enclosed topography and stable atmospheric conditions, where they further
109 combine with polluted air masses transported from the north, resulting in regional and complex air pollution. The Southwest
110 (SW)—spanning the Tibetan Plateau, the Yunnan–Guizhou Plateau, and the Sichuan Basin—is the most topographically and
111 climatically diverse, where topographic confinement and local circulations strongly modulate pollution composition and
112 evolution.

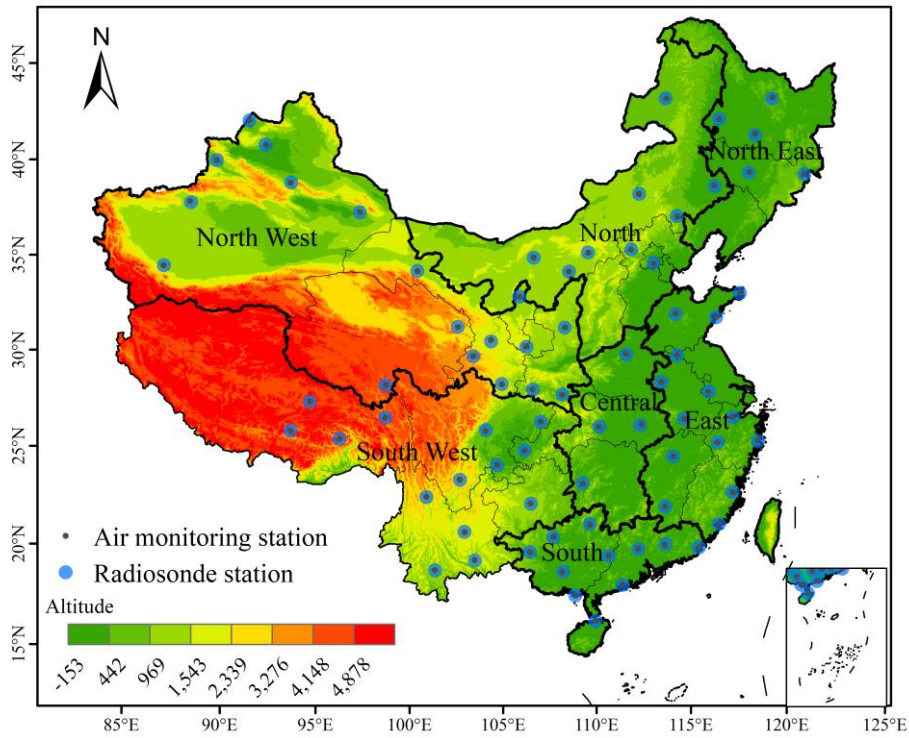


Fig.1 Distribution of 75 radiosonde stations in China. The inset map in the lower right shows the South China Sea Islands.

2.2 Data

Radiosonde observations. We use L-band high-resolution sounding data from the operational network of the China Meteorological Administration (CMA). Since nationwide deployment in 2011, the system has routinely operated ~120 radiosonde stations with standard launches at 08:00 and 20:00 Beijing Time (00:00 and 12:00 UTC), with additional warm-season soundings (May–August) to capture monsoon processes (Guo et al., 2016; Yan et al., 2020). The GTS1 digital radiosonde provides vertical profiles of temperature, pressure, humidity, wind speed, and direction from the surface (0 m AGL) to ~30 km, with 5–8 m nominal vertical resolution (sampling frequency 1.2 s). By integrating in-situ observations from the co-located surface weather station as the initial record, the valid bottom height for all profiles is strictly maintained at 0 m. Independent assessments indicate temperature errors <0.1 K in the troposphere and data quality comparable to internationally recognized radiosondes within the planetary boundary layer (Ma et al., 2010). These measurements have been widely applied to studies of cloud microphysics, PBL height, and inversion detection, and as inputs to numerical weather prediction and atmospheric composition research (Li et al., 2019; Zang et al., 2017; Zhang et al., 2020). For this study (2016–2021), we applied routine quality control to remove obvious temperature/height outliers and used the full-resolution vertical profiles to identify inversion layers and derive their properties.

Surface PM_{2.5} monitoring. Hourly PM_{2.5} concentrations were obtained from the national air-quality monitoring network operated by the China National Environmental Monitoring Centre (CNEMC; real-time platform: <https://www.cnemc.cn/en/>) (Miao et al., 2020; Yan et al., 2020). As of 1 March 2022, the network comprised 2,026 stations with dense coverage in eastern

132 urban clusters and relatively sparse representation in western high-altitude regions. To match radiosonde stations with PM_{2.5}
 133 monitors, we used a distance threshold method with a 10 km search radius. This approach identified 75 valid station pairs,
 134 balancing spatial representativeness and sample size (Fig. 1). The 10 km threshold avoids underrepresentation from smaller
 135 radii and minimizes spatial error from larger distances, representing the point where further increases yield diminishing returns
 136 in matches (the distribution of original sites and the screening method are referenced in Figs S1 and S2.). For temporal
 137 alignment with the soundings, hourly PM_{2.5} records were extracted around 08:00 and 20:00 BJT. Basic completeness checks
 138 and standard plausibility screening were applied before analysis.

139 Rationale for integration. The combination of meter-scale-resolution vertical thermodynamic profiles with collocated
 140 surface PM_{2.5} enables a consistent, observation-based assessment of inversion frequency, intensity, and thickness—and their
 141 diurnal and regional variability—while overcoming the coarse vertical structure inherent in reanalysis products (Li et al., [2019](#);
 142 Yan et al., [2020](#); Zhang et al., [2020](#))

143 3 Method

144 The sounding data underwent manual quality control to identify and systematically remove obvious errors in temperature and
 145 height measurements. Raw temperature profiles were first interpolated using cubic splines to ensure vertical continuity. TIs
 146 were then identified by applying a first-derivative algorithm to the smoothed profiles (Kahl, [1990](#); Serreze et al., [1992](#)). Each
 147 profile was scanned upward from the surface; layers exhibiting a positive vertical temperature gradient were classified as
 148 inversion layers, while those with negative gradients were considered non-inversion zones. The base height of an inversion
 149 layer was defined as the lowest altitude at which temperature began to increase with height, and the top height was identified
 150 as the point where the gradient reverted to negative. Following Kahl et al. ([1996](#)), three fundamental TI parameters were
 151 derived: inversion thickness (ΔH), inversion strength (ΔT), inversion frequency (F_{TI}). They are defined as:

$$152 \quad \Delta H = H_t - H_b \quad (1)$$

$$153 \quad \Delta T = T_t - T_b \quad (2)$$

$$154 \quad F_{TI} = N_{TI}/N \quad (3)$$

$$155 \quad F_{SBI} = N_{SBI}/N \quad (4)$$

$$156 \quad F_{EI} = N_{EI}/N \quad (5)$$

157 where H_t and H_b represent the top and bottom heights of the TI layer respectively; T_t and T_b represent the temperatures
 158 at the top and bottom respectively; N represents the total number of detections, N_{TI} represents the number of detections
 159 where TI occurs, and N_{SBI} and N_{EI} represent the number of detections where SBI and EI occur respectively.

160 To mitigate false positives from small-scale turbulence (e.g., "sawtooth" noise in balloon-borne measurements),
 161 thresholds for ΔH and ΔT were imposed per established practices (Guo et al., [2020](#); Kahl, [1990](#)). A layer was classified as

162 a valid TI only if $\Delta H \geq 100$ m and $\Delta T \geq 0.5^\circ\text{C}$; otherwise, it was discarded. Non-inversion layers embedded within broader
163 TIs were permitted, provided the overarching TI met these criteria. The temperature profile was scanned upward from the
164 surface, and the first continuous layer satisfying $\Delta H \geq 100$ m and $\Delta T \geq 0.5^\circ\text{C}$ was identified as the inversion for that
165 sounding. To specifically target thermodynamic processes influencing surface air quality, this study considers only inversion
166 layers with a base height $H_b \leq 2000$ m. Inversion can also be classified into SBI and EI based on the base height. When H_b
167 < 100 m, it is called Surface-based inversion (SBI); when $100 \text{ m} < H_b \leq 2000$ m, it is called Elevated inversion (EI). For
168 additional validation at different thickness thresholds, please refer to supplementary Figs S18-S20. Theoretical calculations
169 indicate that each station should have a total of 4384 soundings at 12-hour intervals from 2016 to 2021. In practice, however,
170 data omissions occurred due to various factors, resulting in an average missing rate of 3.2% for TI data in the final statistics.

171 According to China's National Ambient Air Quality Standards (GB3095-2012), the standard for a pollution event is based
172 on a daily mean $\text{PM}_{2.5}$ concentration exceeding $75 \mu\text{g m}^{-3}$. In this study, to align with the instantaneous radiosonde observations
173 at 08:00 and 20:00 BJT, we applied this concentration threshold $75 \mu\text{g m}^{-3}$ to the hourly $\text{PM}_{2.5}$ data to identify pollution events
174 corresponding to the sounding times. $\text{PM}_{2.5}$ concentrations are further classified into six categories: Excellent: $0\text{-}35 \mu\text{g m}^{-3}$;
175 Good: $35\text{-}75 \mu\text{g m}^{-3}$; Light pollution: $75\text{-}115 \mu\text{g m}^{-3}$; Moderate pollution: $115\text{-}150 \mu\text{g m}^{-3}$; Severe pollution: $150\text{-}250 \mu\text{g m}^{-3}$;
176 Extreme pollution: $>250 \mu\text{g m}^{-3}$. To align with the spatiotemporal characteristics of the radiosonde data, the hourly $\text{PM}_{2.5}$ data
177 were processed into two time periods corresponding to the radiosonde observations: 08:00 and 20:00 Beijing Time.

178 **4 Results and Discussions**

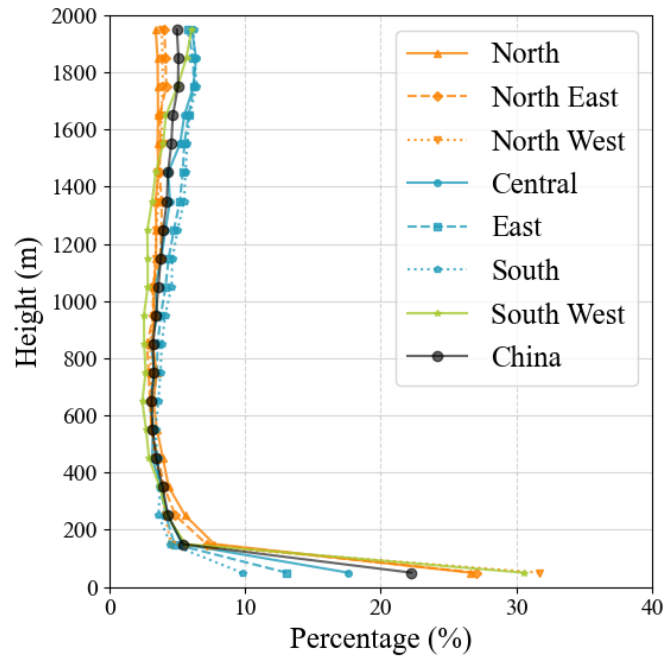
179 **4.1 Spatiotemporal distribution of atmospheric temperature inversions in China**

180 The base height of TI sets the effective lid for vertical pollutant dispersion. To resolve its vertical structure within the boundary
181 layer, we quantified the vertical distribution of inversion events. This is defined as the percentage of the total number of
182 inversion events falling within each 100-m height bin from the surface to 2 km (Fig. 2). A distinct non-linear profile emerges:
183 the TI proportion peaks sharply in the lowest 0–100 m bin, which comprises exclusively SBIs and accounts for 22.2% of all
184 inversion events. This peak is followed by a rapid decline to a minimum of 3.1% at 600–700 m, and then a gradual recovery
185 to 5.1% at 1800–1900 m—i.e., a “rapid decline, then slow recovery” with height.

186 Marked regional contrasts accompany this vertical pattern. In the near-surface layer (0–100 m, i.e., the SBI), the Northwest
187 exhibits the highest TI proportion 31.6%, followed by Southwest 30.5%. In comparison, Central, East, and South China show
188 lower near-surface SBI proportions, with South China the lowest 9.8%. The pattern reverses aloft: for elevated inversions in
189 the 1000–2000 m layer, South China records the highest proportion 56.0%, whereas northern regions are much less affected.
190 Taken together, intense near-surface trapping by SBIs preferentially occurs over inland northern and southwestern China, while
191 EIs are more common and reach higher altitudes in the southeastern coastal belt. A potential driver of this dipole is the diurnal

192 temperature range (DTR): larger DTRs over inland regions enhance nocturnal radiative cooling, favoring strong SBIs; weaker
193 DTRs in maritime-influenced southeastern areas favor synoptic processes that produce EIs.

194



195

196

Fig.2 Vertical distribution of inversion base height: fraction of total inversions per height bin.

197

198 4.1.1 Inversion frequency

199

200

201

202

203

204

205

206

207

208

209

210

211

212

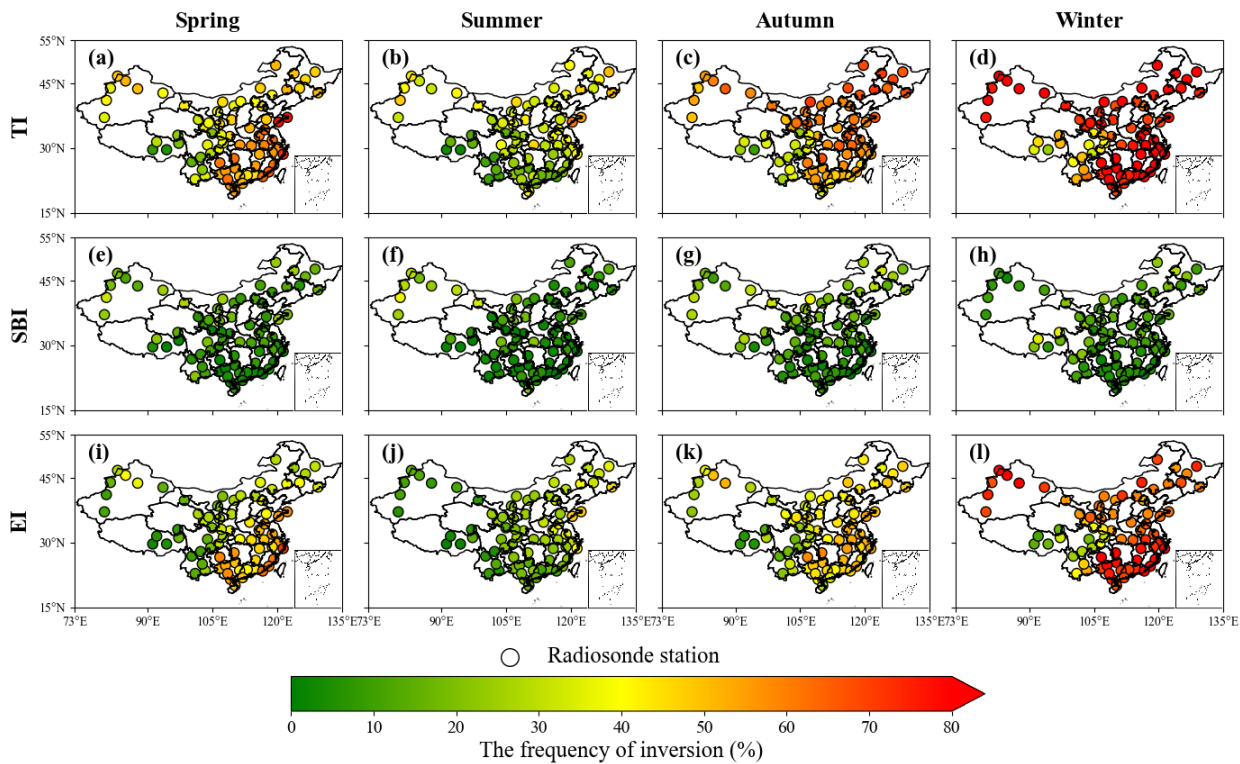
Figure 3 maps the spatial and seasonal variability of TI frequency over China (2016–2021), revealing pronounced regional heterogeneity. High TI occurrence is concentrated along the coasts (East and South China) and across northern China (Northeast, North, Northwest), yielding a national annual mean of 54.9%. Regionally, Northeast China records the highest frequency (59.5%), whereas the Southwest exhibits the lowest (31.3%; Table 1). The suppressed occurrence in the Southwest likely reflects two factors: (i) in the Sichuan Basin, the dominant signal is lower-tropospheric inversions (LTIs) which typically occur at altitudes of 2,200–3,400 m—well above the 0–2,000 m height range examined in this study—resulting in their exclusion from our frequency statistics, and (ii) plateau climate conditions—high elevation, strong solar radiation, low air density, and frequent strong winds linked to the westerly jet—enhance turbulent mixing and disrupt inversion persistence (Feng et al., 2020; Schiemann et al., 2009). National averages by type indicate SBIs ~13% and EIs ~43% annually (Figs. 4d, 4g). EIs dominate total events nationally. The two inversion types exhibit contrasting geography: SBIs cluster over northern China (Northeast, North, Northwest) with annual frequencies of 14.9–16.1%, whereas EIs prevail across the southeastern coastal and central regions (South, East, Central China), averaging 48.1% and peaking at 51.6% in East China. This spatial dipole aligns with previous radiosonde climatologies, which report more frequent SBIs in northern/western China and EI dominance in the south and east (Huang et al., 2021). A persistent “east-high, west-low” gradient is also evident. One contributing factor is the

213 fixed launch time relative to local solar time: China spans roughly five time zones, so the 08:00 BJT sounding corresponds to
214 ~05:00 local time in the far west, when nocturnal inversions may not yet have fully developed, biasing frequencies lower there.

215 Figure 4a shows pronounced seasonality in TI occurrence. The highest monthly means occur at 08:00 BJT in January
216 (84.0%) and at 20:00 BJT in December (68.8%), whereas minima appear in June (31.9%) and August (32.0%). SBI occurrence
217 shows relatively high frequencies (>24%) in February, March, September, and October, whereas EI frequency exhibits a sharp,
218 single peak in January (75.2%). Seasonal contrasts are stark: inversions are most frequent in the cold season and relatively rare
219 in the warm season. The spatial footprint of inversion-prone areas expands westward from summer to winter: in summer, only
220 the Northeast exceeds 40%, and the Southwest falls to 17.5%; in winter, all regions except the Southwest surpass 70%, reaching
221 80.5% in the Northeast. SBIs and EIs share this seasonal phasing—winter maxima, summer minima—consistent with longer
222 winter nights that enable sustained radiative cooling and stronger stability.

223 Further analysis (Figs. S5, S6 and 4a) shows a robust dawn–dusk asymmetry: inversions are more likely to occur at 08:00
224 BJT across all regions and seasons, with daytime launches accounting for 62% of all TI detections. The contrast is strongest
225 in summer, when 08:00 inversions comprise 71% of events, and weaker in winter (57%). This seasonal modulation reflects
226 differences in solar forcing. In summer, long days and short nights curtail both the formation window and stability of inversions:
227 with sunrise near 05:20 BJT, 2–3 hours of insolation have already eroded the nocturnal layer by 08:00, and by 20:00 roughly
228 12 hours of high-angle solar heating have largely dissipated residual stability—yielding a 26.4% frequency gap between the
229 two launch times. In winter, short days and long nights promote the development of deeper and more persistent inversions
230 through enhanced radiative cooling. With sunrise as late as around 07:20 BJT, the weak early-morning insolation preceding
231 the 08:00 sounding is insufficient to dissipate the TI layer significantly. Furthermore, the wintertime atmosphere is significantly
232 drier (Fig. S7), which minimizes downward longwave radiation and thereby maximizes the efficiency of nocturnal surface
233 cooling. The subsequent ~10 hours of low-angle daylight provide insufficient thermal energy to significantly disturb the stable
234 surface layer before 20:00. Consequently, the 08:00–20:00 frequency difference contracts to 14.8% in winter.

235

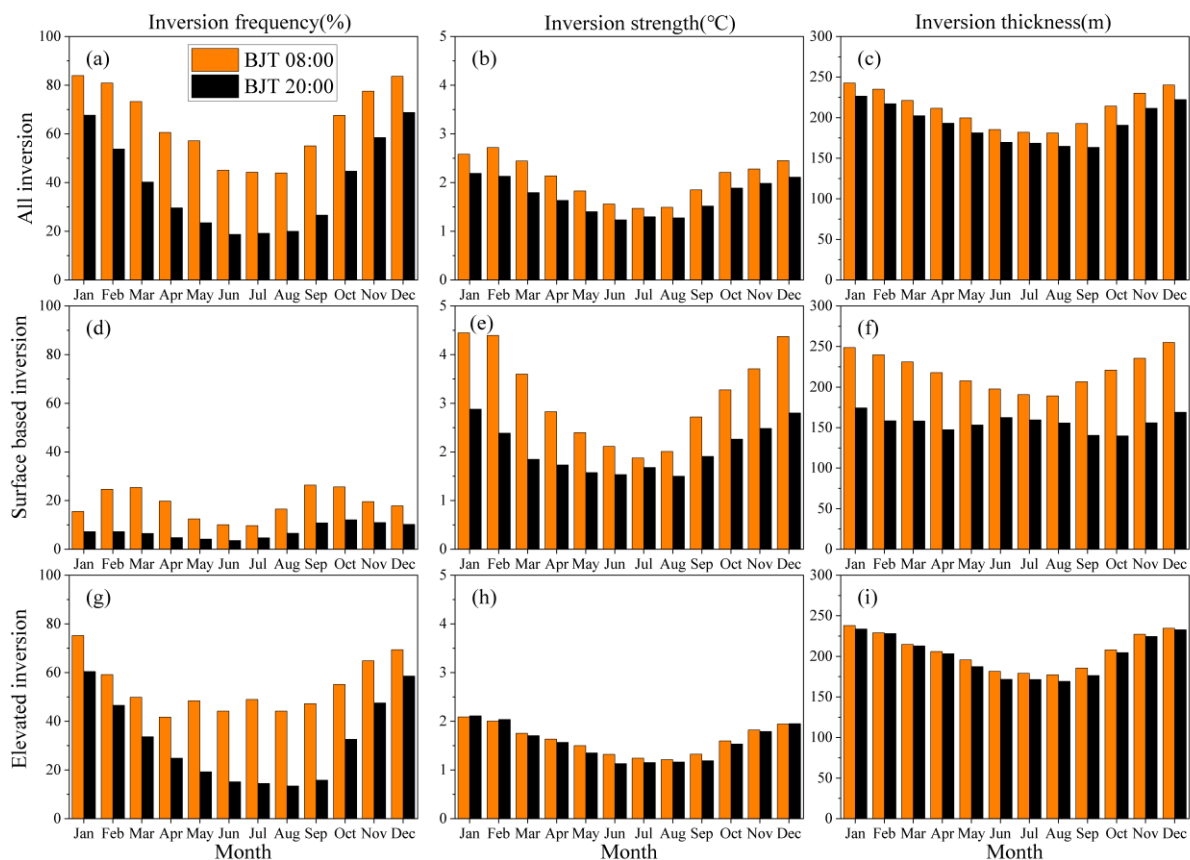


236

237 Fig. 3. Spatial and seasonal distribution of occurrence frequency for different types of TI. For more details about SBI, please refer to Fig.

238 S15.

239



240

241

Fig. 4 Monthly variations of TI parameters in China (2016–2021).

242

Table 1. Annual mean values of TI parameters by region.

Region	TI			SBI			EI		
	$F_{TI}(\%)$	$\Delta T(^{\circ}\text{C})$	$\Delta H(\text{m})$	$F_{SBI}(\%)$	$\Delta T(^{\circ}\text{C})$	$\Delta H(\text{m})$	$F_{EI}(\%)$	$\Delta T(^{\circ}\text{C})$	$\Delta H(\text{m})$
Central	57.0	2.08	231	10.0	3.54	213	47.0	1.80	235
East	59.3	1.86	217	7.7	2.54	197	51.6	1.74	219
North	55.8	2.20	201	14.9	3.72	204	40.9	1.63	199
North East	59.5	2.11	211	16.1	3.34	210	43.4	1.63	212
North West	49.3	2.67	215	15.8	3.91	209	33.5	1.92	218
South	50.7	1.92	222	5.0	1.74	186	45.7	1.93	227
South West	31.3	2.05	202	9.6	2.39	186	21.7	1.66	202

244

245 **4.1.2 Inversion strength**

246 Among the key TI parameters, strength exerts first-order control on pollutant dispersion. Spatially, TI strength is greater over
247 inland northern regions than over southern and eastern coasts (Fig. 5; Table 1): the Northwest has the highest annual mean
248 (2.67 °C), whereas the East is lowest (1.86 °C). Extremes span 4.69 °C in the Southwest to 1.67 °C in the East. Seasonally, TI
249 strength peaks in winter (2.44 °C), weakens in spring and autumn (both ~2.10 °C), and is lowest in summer (1.53 °C) (Fig. 5).
250 Monthly values maximize in February (2.73 °C) and minimize in June (1.23 °C) (Fig. 4b). By inversion type, SBIs are
251 consistently stronger than EIs: peak intensities reach 4.45 °C (SBI) versus 2.11 °C (EI) (Figs. 4e, 4h). Correspondingly, annual
252 means rank SBI (3.02 °C) > all TI (2.13 °C) > EI (1.76 °C). The strongest seasonal maxima occur in winter in the Northwest
253 for both overall TI (2.78 °C) and SBI (4.88 °C), while EI intensity peaks in winter in the South (2.43 °C). Notably, winter SBI
254 strength exceeds EI by more than a factor of two. Geographically, SBI intensity varies substantially—annual means in northern
255 and northwestern China are over twice those in the south—whereas EI strength is comparatively uniform, ranging from 1.63 °C
256 (North/Northeast) to 1.93 °C (South), a spread of only 0.30 °C. Diurnally, TI, SBI, and EI intensities are generally higher at
257 08:00 BJT than at 20:00 (Figs. 4b, 4e, 4h). EI shows a regional reversal: daytime-stronger in the Northeast/North, but
258 nighttime-stronger elsewhere. The maximum values by category occur at 08:00 in the Northwest for all TI (2.81 °C), 08:00 in
259 the North for SBI (4.30 °C), and 20:00 in the South for EI (2.02 °C) (Tables S2, S3).

260

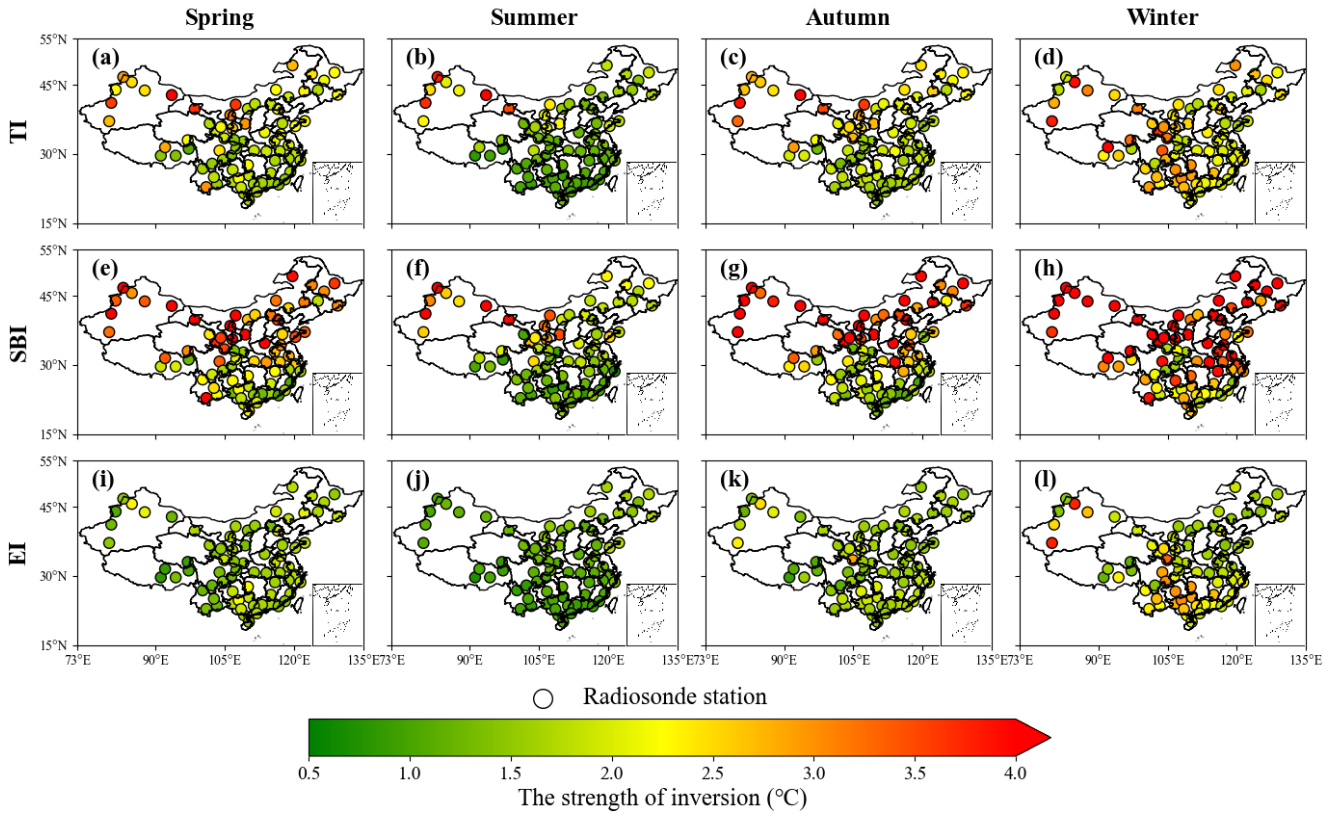


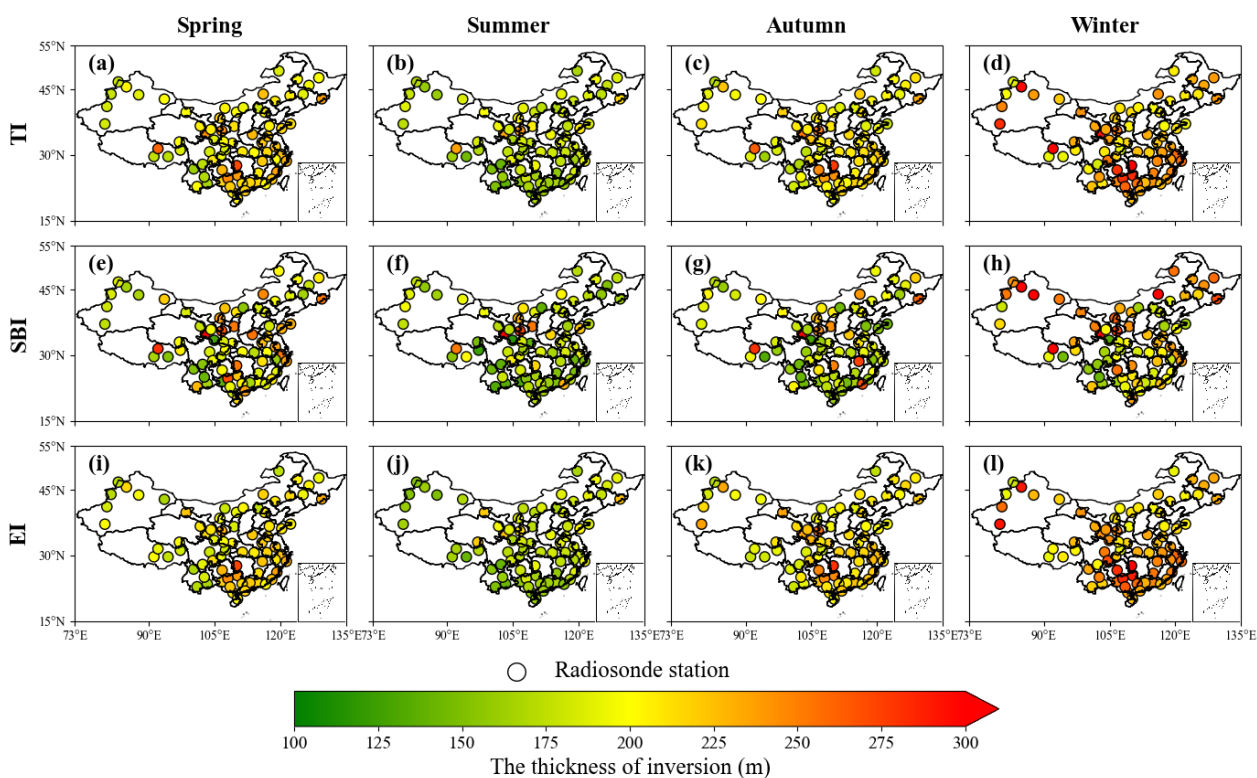
Fig.5 Spatial and seasonal distribution of inversion strength for different types of inversions.

4.1.3 Inversion thickness

Seasonal and regional patterns of inversion thickness for all TIs, SBIs, and EIs are shown in Figure 6 and summarized in Table 1. Across the 75 radiosonde stations, the annual mean thickness is 214 m. Layers sampled at 08:00 BJT are generally thicker than those at 20:00 BJT by about 40 m, consistent with the diurnal phasing of inversion intensity. Thickness varies markedly by season, maximizing in winter (231 m; Fig. 6d) and minimizing in summer (179 m; Fig. 6b). Monthly evolution follows a pronounced “V” shape (Fig. 4c), with a January peak of 243 m. By type, EIs are systematically thicker than SBIs, with annual means of 216 m and 201 m, respectively. Both exhibit winter maxima and summer minima. At 08:00, EI and SBI each display a clear “V”-shaped monthly cycle, whereas at 20:00 their behavior diverges: SBI thickness varies only modestly, while EI thickness remains comparatively stable across months (Figs. 4f, 4i). Spatially, TIs are notably thicker in the eastern and southern regions compared to the northern and western inland areas. Specifically, the average thickness in East, South, and Central China is 223 m, whereas it is 209 m in Northeast, North, and Northwest China. South China shows the largest annual mean thickness (231 m), exceeding the national mean, whereas the Southwest has the thinnest layers (202 m). This pattern aligns with the regional predominance of inversion types: thicker EIs prevail in the eastern/southern regions, while thinner SBIs are more common in the western/northern regions. The lower overall inversion frequency in the Southwest, combined with the intrinsic thickness contrast between EI and SBI, further contributes to these regional differences. Additionally, we

279 discussed the scenario where the lapse rate ($\Delta T/\Delta H$) was used as a proxy for inversion strength, as elaborated in supplementary
 280 Fig. S16, S17 and Table. S4.

281



282

283 Fig.6 Spatial and seasonal distribution of inversion thickness for different types of inversions.

284

285 4.2 The correlation between temperature inversion and PM_{2.5}

286 4.2.1 Statistical relationship between temperature inversion and PM_{2.5} pollution events

287 We quantified the linkage between TIs and PM_{2.5} pollution by comparing the share of polluted days under inversion versus
 288 non-inversion conditions in each region (Table 2). At 08:00 BJT, a strong association emerges nationwide: co-occurrence rates
 289 span 84.6% in the Northeast (NE) to 62.9% in the Southwest (SW), indicating that morning pollution accumulation is
 290 substantially conditioned by inversions, with northern regions particularly sensitive—consistent with their higher prevalence
 291 of SBIs. By contrast, at 20:00 BJT the TI–PM_{2.5} coupling weakens markedly; the SW shows the lowest overlap, with only
 292 27.7% of pollution events coinciding with inversions. This pronounced diurnal asymmetry suggests distinct formation regimes:
 293 daytime/morning pollution is frequently meteorology-limited by inversion trapping, whereas evening pollution is more
 294 strongly governed by emission timing and chemical processes than by boundary-layer stability.

295

296

297

Table 2. Frequency statistics of TI corresponding to PM_{2.5} pollution events in seven regions of China from 2016 to 2021.

Region	BJT 08:00				BJT 20:00			
	Pollution	Inversion	No-inversion	Inversion proportion	Pollution	Inversion	No-inversion	Inversion proportion
Central	1818	1489	329	81.9%	1713	1027	686	60.0%
East	3239	2672	567	82.5%	3004	1910	1094	63.6%
North	1749	1394	355	79.7%	1433	773	660	53.9%
North East	1072	907	165	84.6%	709	480	229	67.7%
North West	5409	4443	966	82.1%	4734	2299	2435	48.6%
South	1194	891	303	74.6%	881	464	417	52.7%
South West	2523	1586	937	62.9%	2186	608	1578	27.7%

299

300 Figure 7a reveals strong seasonal heterogeneity. Winter registers the most pollution events (17,540), exceeding spring, autumn,
301 and summer by factors of 2.7, 3.2, and 13.8, respectively. TIs substantially amplify this seasonal contrast: relative to no-
302 inversion conditions, the probability of a pollution event rises by +52% in winter, +34% in autumn, +10% in spring, and is
303 negligible in summer. The muted summer response likely reflects a shift toward ozone-dominated chemistry, weakening the
304 coupling between PM_{2.5} and inversion dynamics. Figure 7b shows that TIs not only increase occurrence but also severity—
305 especially in winter—doubling extreme events (Level 4: 2% → 4%) and raising severe events (Level 3) by 3 percentage
306 points (15% → 18%). These observations are consistent with the inversion-driven explosive growth conceptual model for
307 PM_{2.5} (Zhong et al., [2017](#), 2018) and with the view that extreme haze is tightly linked to inversion meteorology (Yang and
308 Shao, [2021](#)). Autumn TIs exhibit a similar but weaker intensification (+3% in moderate/severe categories), whereas spring and
309 summer TIs chiefly affect lower-severity bins. Collectively, the results establish TIs as a critical wintertime meteorological
310 driver of both the frequency and intensity of haze in China.

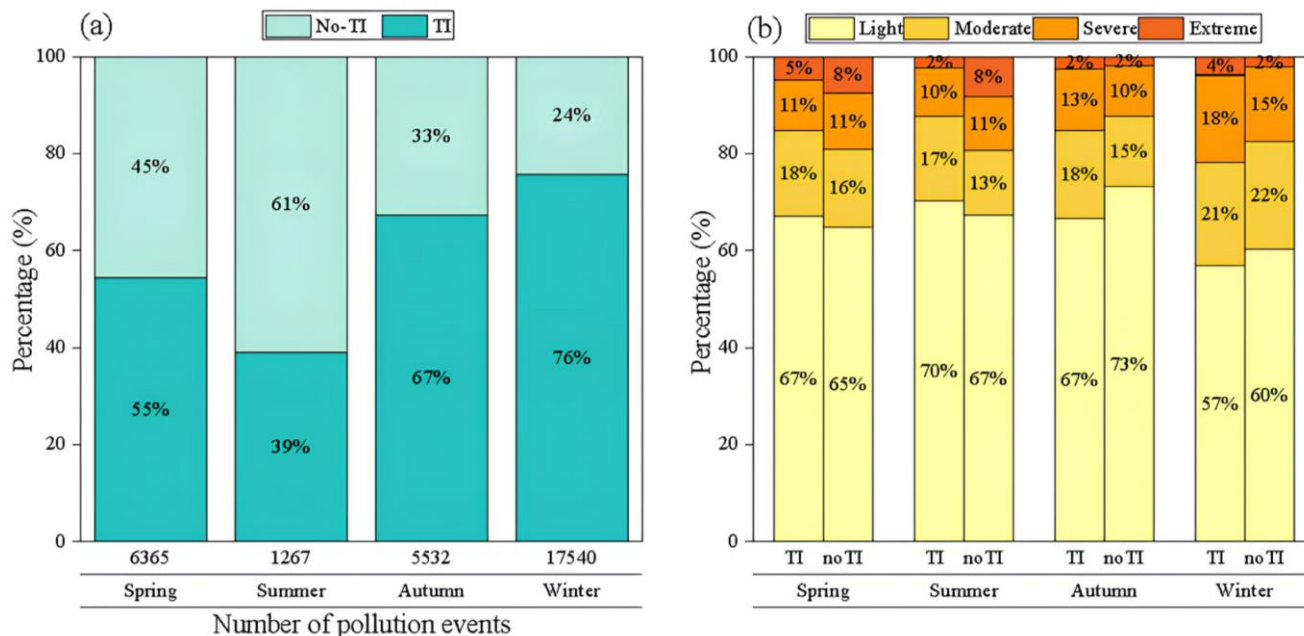


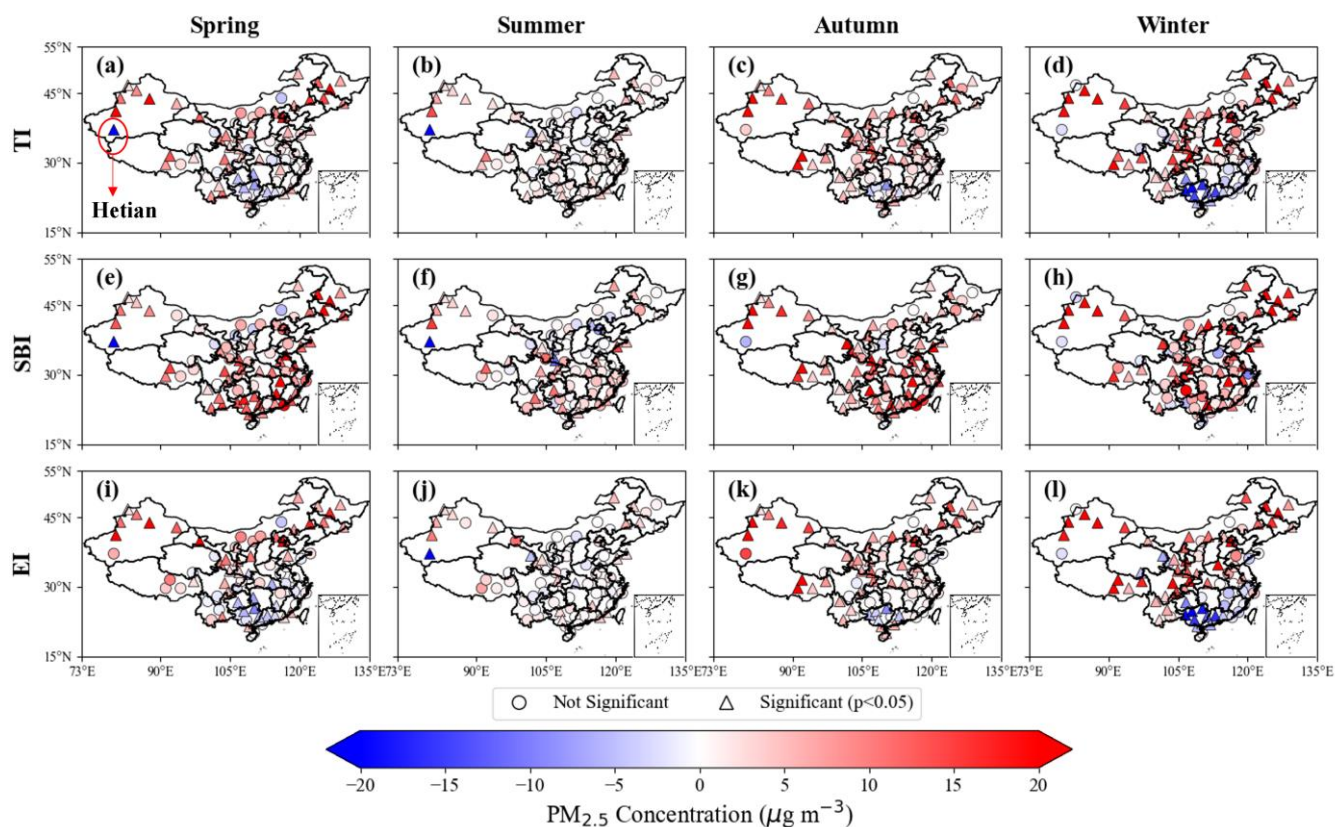
Fig. 7 (a) Frequency of inversion occurrence during polluted periods and (b) distribution of pollution levels in China (2016–2021).

4.2.2 Impacts of different TI types on PM_{2.5} concentrations

We quantify inversion impacts by contrasting the daily mean PM_{2.5} concentrations under inversion and non-inversion conditions, with statistical significance assessed using two-sample t-tests (Fig. 8). The time-resolved analyses for 08:00 and 20:00 BJT are shown in Figs. S12 and S13. In eastern China, results broadly align with Shao et al. (2023): PM_{2.5} increases significantly under inversions in the Northeast (NEC) and North China (NC), whereas South China (SC) exhibits significant decreases. In western China, most stations also show PM_{2.5} enhancements during inversions, with a notable exception at Hetian (southern Xinjiang), where spring–summer concentrations decline significantly (Figs. 8a, 8b). This anomaly likely reflects the dust-dominated composition of PM_{2.5} (>90%) and frequent spring–summer dust storms near the Taklamakan Desert; strong winds that accompany dust events are unfavorable for inversion formation, rendering dust outbreaks and inversion episodes largely mutually exclusive (Aishajiang et al., 2020). Consequently, during inversion periods, the dominant dust component is largely absent, yielding lower PM_{2.5}.

Disaggregating by inversion type reveals fundamentally different mechanisms. Surface-based inversions (SBIs) robustly increase PM_{2.5} across most regions—especially in winter and autumn (Figs. 8g, 8h)—consistent with nocturnal radiative cooling that produces a shallow, stable layer, suppresses vertical mixing, and accelerates near-surface accumulation (Stull, 1988; Zhong et al., 2017). The amplification in northern winters reflects longer nights and stronger surface cooling. By contrast, elevated inversions (EIs) exhibit spatially variable effects: they enhance PM_{2.5} in NEC, NC, and Northwest China (NWC), but reduce concentrations in SC. This pattern supports the hypothesis that EIs can inhibit pollutant transport (Yang and Shao, 2021): in SC, EIs often accompany synoptic subsidence or warm advection, establishing a capping layer that limits vertical exchange and isolates the region from northerly inflow. Such a transport-suppression mechanism is less relevant in northern

332 China, where local emissions dominate. Diurnal contrasts further modulate these responses: morning (08:00) inversions
 333 generally exert stronger effects than evening (20:00) inversions, particularly in NWC (Figs. S12, S13). Occasional nighttime
 334 $PM_{2.5}$ decreases under SBIs are observed at some NC/NEC stations, but these changes are not statistically significant.
 335

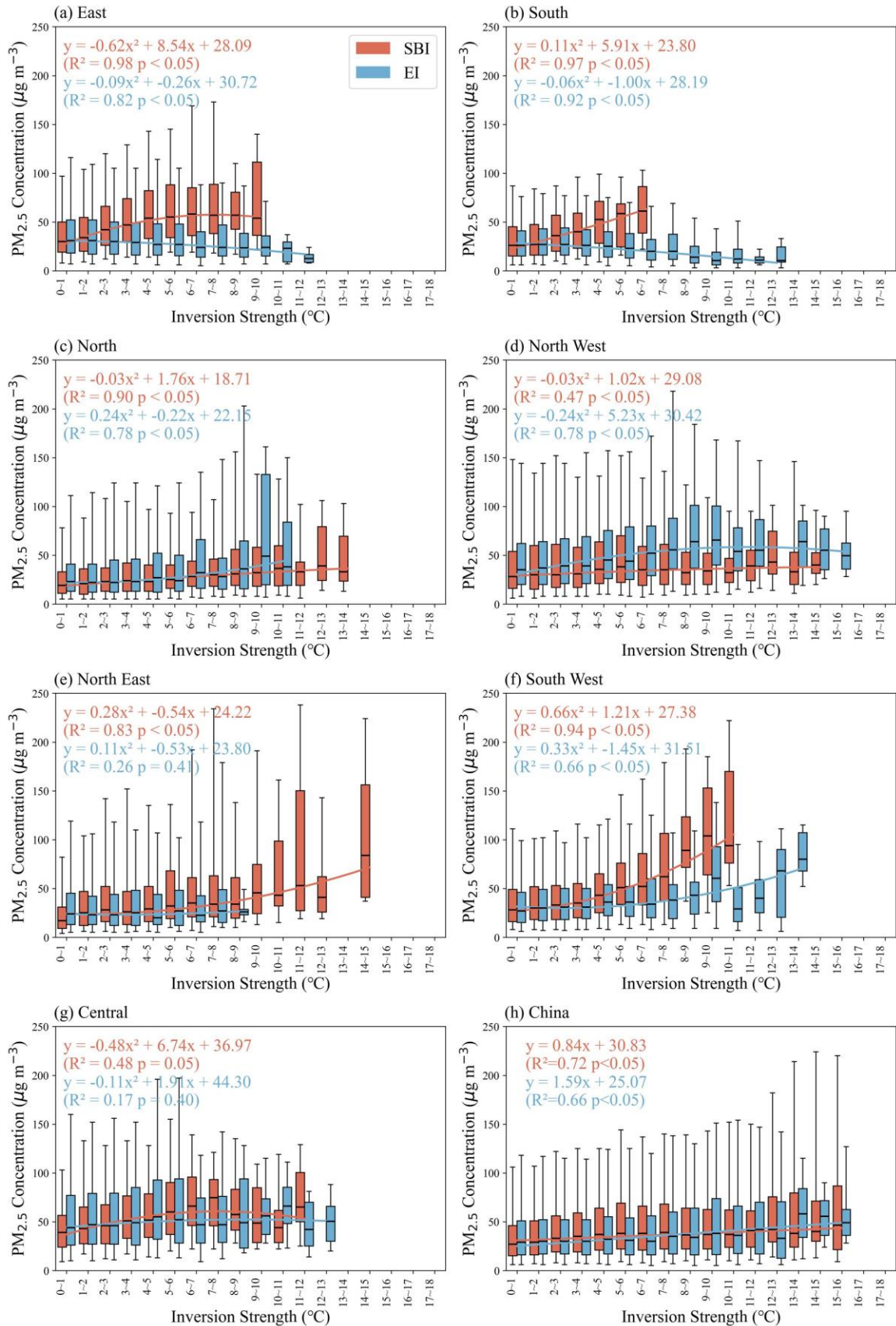


336
 337 Fig.8 Distribution of $PM_{2.5}$ concentration differences with and without TI. The larger circle indicates significance at the 95% level (t -test)
 338

339 We quantified $PM_{2.5}$ responses to inversion parameters (strength, thickness) at 75 stations. Nationwide, $PM_{2.5}$ rises near-
 340 linearly with inversion strength for both SBIs and EIs (Fig. 9h): below 8 °C, SBIs exert the stronger effect; above 8 °C, EIs
 341 become more influential. Regionally, four response regimes emerge: Northern Inland China, Southeastern Coastal China,
 342 Central China, and Southwestern China. In EC/SC, SBI intensity correlates positively with $PM_{2.5}$ ($R^2 > 0.9$), whereas EI
 343 intensity correlates negatively ($R^2 > 0.8$); SBI strengths there seldom exceed 10 °C, far weaker than inland values. In NEC/NC,
 344 SBI strength can exceed 14 °C and is strongly coupled to $PM_{2.5}$. EI effects are mixed: NC shows a monotonic increase in $PM_{2.5}$
 345 with EI strength; NWC peaks at 10.9 °C ($58.9 \mu\text{g m}^{-3}$) then declines; NEC shows no significant correlation. In the SWC, both
 346 SBI and EI display a parabolic relationship with $PM_{2.5}$, with SBI exerting the larger enhancement (correlation up to 0.94). In
 347 Central China, overall fits are poor/non-significant, likely reflecting (i) the limited sample (four stations) and (ii) the region's
 348 role as a convergence zone receiving substantial inflow from surrounding regions—regional transport contributes >65% to
 349 $PM_{2.5}$ in cities such as Wuhan (Yu et al., 2020).

350 By contrast, inversion thickness shows a much weaker and less uniform association with $PM_{2.5}$ (Fig. S14). SBI thickness

351 is generally positively correlated with $PM_{2.5}$ (except in NEC). For EI, significant thickness- $PM_{2.5}$ relationships appear only in
352 NEC and NWC ($R^2 = 0.86$ and 0.92 , respectively); elsewhere, EI thickness exerts negligible influence. Together, these results
353 establish inversion strength—not thickness—as the dominant predictor of $PM_{2.5}$ accumulation (Fig. 9 vs. Fig. S14). Thickness
354 primarily defines the volume of the trapping layer: a deep but weak inversion can be eroded by mechanical turbulence more
355 readily than a shallow but intense one. This mechanism ensures that a stronger temperature gradient yields greater static
356 stability and more effective suppression of turbulent mixing (Liu et al., [2022](#)).



357

358 Fig.9 Fitting relationship between inversion strength and PM_{2.5} concentration across seven regions of China from 2016 to 2021. The ends of

359 the boxes, the ends of the bars, and the short line across each box represent the 25th and 75th percentiles, the 5th and 95th percentiles, and

360 the median, respectively. Each strength interval contains a sample size ≥ 10 .

361 **5 Conclusions**

362 Temperature inversions (TIs) are widely recognized as a key meteorological regulator of near-surface $PM_{2.5}$, yet their
363 nationwide behaviour and impacts have remained incompletely characterized. Leveraging high-vertical-resolution radiosondes
364 from 75 stations (2016–2021) and collocated surface $PM_{2.5}$, we provide an observation-based assessment of inversion
365 frequency, intensity, thickness, and diurnal variability across China, and quantify how distinct inversion types modulate
366 pollution accumulation.

367 First, TIs are pervasive: the national annual means are 51.8% for frequency, 2.13 °C for strength, and 214 m for thickness.
368 Strong regional heterogeneity emerges. SBIs occur more frequently and are substantially stronger over inland northern regions
369 (annual mean 3.02 °C), whereas EIs prevail along the southeastern coast and are thicker (e.g., 235 m in Central China; 227 m
370 in South China). Low-level inversions are comparatively rare in the Southwest. Diurnally, inversions are more frequent,
371 stronger, and thicker at 08:00 BJT than at 20:00, with the SBI day–night contrast muted in summer and amplified in winter—
372 consistent with radiative control. Second, TIs materially elevate winter haze risk. Relative to non-inversion conditions, the
373 probability of a pollution event increases by 52% in winter, and the share of extreme events doubles, establishing TIs as a first-
374 order meteorological driver of both frequency and severity of winter haze in China. Third, the type of inversion matters. SBIs
375 robustly enhance $PM_{2.5}$ across most regions, reflecting efficient near-surface trapping under nocturnal stability. EIs show
376 regionally divergent behaviour: they enhance $PM_{2.5}$ in the north and northwest but are negatively associated with $PM_{2.5}$ in the
377 east and south, consistent with a transport-inhibition mechanism that limits northerly inflow under subsidence/warm-advection
378 regimes. Fourth, inversion strength is the dominant predictor of $PM_{2.5}$ accumulation, while thickness plays a secondary, region-
379 dependent role. Nationally, $PM_{2.5}$ increases near-linearly with strength for both SBI and EI; below 8 °C SBI effects dominate,
380 whereas above 8 °C EI effects strengthen. Thickness is generally weakly correlated with $PM_{2.5}$, except in select regions (e.g.,
381 NEC/NWC for EI), underscoring that static stability (temperature gradient) governs ventilation more directly than layer depth.

382 These findings offer concrete avenues for improving air pollution forecasting. (i) Improving the vertical resolution and
383 the predictive skill of TIs in numerical models could enhance the forecast of air pollution events, particularly in winter. (ii)
384 Region-specific strategies are warranted: curbing evening–night emissions and promoting nocturnal ventilation are likely most
385 effective where SBIs dominate (northern basins/plains), whereas transport management and synoptic-regime awareness may
386 be more impactful in the southeast where EIs can isolate the boundary layer from upwind inflow. (iii) The observed diurnal
387 asymmetry suggests targeted mitigation during windows of maximum trapping (pre-sunrise to morning transition).

388 Our assessment remains limited by sparser coverage over plateau terrain and the lack of vertical $PM_{2.5}$ profiles, which
389 constrains diagnosis of aerosol layering and entrainment. Future work should augment radiosondes with Raman/HSRL lidar,
390 UAV or aircraft soundings, and assimilate inversion-aware stability metrics into kilometre-scale chemical transport models;
391 leverage geostationary multi-sensor diurnal sampling to resolve inversion evolution; and evaluate co-trends among inversions,

emissions, and climate-driven shifts in nocturnal cooling and synoptic patterns. These steps will sharpen causal attribution of TI–pollution coupling and strengthen the forecast-to-policy pipeline for region-tailored air-quality management.

Data availability. The radiosonde data used in this study are available from the China Meteorological Administration (CMA). The hourly ground-level PM_{2.5} concentration data can be obtained from the China National Environmental Monitoring Centre (CNEMC; real-time platform: <https://www.cnemc.cn/en/>).

Author contributions. YF and HW designed the study. HH, JG, XZ and FM contributed to the observation data, provided experimental assistance, and analyzed the methodology. YF wrote the paper with input from all the other authors.

Competing interests. The authors declare that they have no known competing financial interests or personal relationships that could have appeared to influence the work reported in this paper.

Acknowledgements. This study was funded by the Sichuan Provincial Central Leading Local Science and Technology Development Special Project (2025ZYD0179), the "Challenge and Command" China Meteorological Administration (CMAJBGS202607), the Open Grants of China Meteorological Administration Radar Meteorology Key Laboratory (2025ZD02), the Innovation Fund of the Jilin Field Research Station for Cloud Physics, China Meteorological Administration/Jilin Provincial Key Laboratory of Weather Modification (M202504), and the Key Laboratory of Intelligent Meteorological Observation Technology, China Meteorological Administration (ZNGC2025MS21).

Financial support. This research has been supported by the Sichuan Provincial Central Leading Local Science and Technology Development Special Project (2025ZYD0179), the "Challenge and Command" China Meteorological Administration (CMAJBGS202607), the Open Grants of China Meteorological Administration Radar Meteorology Key Laboratory (2025ZD02), the Innovation Fund of the Jilin Field Research Station for Cloud Physics, China Meteorological Administration/Jilin Provincial Key Laboratory of Weather Modification (M202504), and the Key Laboratory of Intelligent Meteorological Observation Technology, China Meteorological Administration (ZNGC2025MS21).

References

- Aishajiang, A., Liang, F., Xu, H., Muhetaer, W., and Maimaitiaili, M.: Transport pathway of dust storm and its impact on air quality in Hetian Oasis, *Acta Scientiae Circumstantiae*, 40, <https://doi.org/10.13671/j.hjkxxb.2020.0159>, 2020.
- Chan, C. K. and Yao, X.: Air pollution in mega cities in China, *Atmospheric Environment*, 42, 1–42,

- 423 <https://doi.org/10.1016/j.atmosenv.2007.09.003>, 2008.
- 424 Chen, J., Lv, H., Wang, Q., Wang, G., Jia, K., Zhao, C., Shi, W., and Yan, X.: Revolutionizing Satellite Real-Time Air Pollution
425 Alerts through New On-Orbit System-on-Chip Technology, *Environ. Sci. Technol.*, 59, <https://doi.org/10.1021/acs.est.5c02470>,
426 2025.
- 427 Czarnecka, M., Nidzgorska-Lencewicz, J., and Rawicki, K.: Temporal structure of thermal inversions in Leba (Poland), *Theor
428 Appl Climatol*, 136, 1–13, <https://doi.org/10.1007/s00704-018-2459-8>, 2019.
- 429 Deng, C., Qin, C., Li, Z., and Li, K.: Spatiotemporal variations of PM_{2.5} pollution and its dynamic relationships with
430 meteorological conditions in beijing-tianjin-hebei region, *Chemosphere*, 301, 134640,
431 <https://doi.org/10.1016/j.chemosphere.2022.134640>, 2022.
- 432 Feng, X., Wei, S., and Wang, S.: Temperature inversions in the atmospheric boundary layer and lower troposphere over the
433 Sichuan Basin, China: Climatology and impacts on air pollution, *Science of The Total Environment*, 726, 138579,
434 <https://doi.org/10.1016/j.scitotenv.2020.138579>, 2020.
- 435 Garcia, A., Santa-Helena, E., De Falco, A., De Paula Ribeiro, J., Gioda, A., and Gioda, C. R.: Toxicological Effects of Fine
436 Particulate Matter (PM_{2.5}): Health Risks and Associated Systemic Injuries—Systematic Review, *Water Air Soil Pollut*, 234,
437 <https://doi.org/10.1007/s11270-023-06278-9>, 2023.
- 438 Guo, J., Miao, Y., Zhang, Y., Liu, H., Li, Z., Zhang, W., He, J., Lou, M., Yan, Y., Bian, L., and Zhai, P.: The climatology of
439 planetary boundary layer height in China derived from radiosonde and reanalysis data, *Atmos. Chem. Phys.*, 16, 13309–13319,
440 <https://doi.org/10.5194/acp-16-13309-2016>, 2016.
- 441 Guo, J., Chen, X., Su, T., Liu, L., Zheng, Y., Chen, D., Li, J., Xu, H., Lv, Y., He, B., Li, Y., Hu, X.-M., Ding, A., and Zhai, P.:
442 The Climatology of Lower Tropospheric Temperature Inversions in China from Radiosonde Measurements: Roles of Black
443 Carbon, Local Meteorology, and Large-Scale Subsidence, *Journal of Climate*, 33, 9327–9350, [https://doi.org/10.1175/JCLI-
D-19-0278.1](https://doi.org/10.1175/JCLI-
444 D-19-0278.1), 2020.
- 445 Huang, Q., Chu, Y., and Li, Q.: Climatology of low-level temperature inversions over China based on high-resolution
446 radiosonde measurements, *Theor Appl Climatol*, 144, 415–429, <https://doi.org/10.1007/s00704-021-03536-w>, 2021.
- 447 Kahl, J. D.: Characteristics of the low-level temperature inversion along the Alaskan Arctic coast, *Intl Journal of Climatology*,
448 10, 537–548, <https://doi.org/10.1002/joc.3370100509>, 1990.
- 449 Kahl, J. D. W., Martinez, D. A., and Zaitseva, N. A.: Long-term variability in the low-level inversion layer over the arctic
450 ocean, *Int. J. Climatol.*, 16, 1297–1313, [https://doi.org/10.1002/\(SICI\)1097-0088\(199611\)16:11%253C1297::AID-
JOC86%253E3.0.CO;2-T](https://doi.org/10.1002/(SICI)1097-0088(199611)16:11%253C1297::AID-
451 JOC86%253E3.0.CO;2-T), 1996.
- 452 Kassomenos, P. A., Paschalidou, A. K., Lykoudis, S., and Koletsis, I.: Temperature inversion characteristics in relation to
453 synoptic circulation above Athens, Greece, *Environ Monit Assess*, 186, 3495–3502, [https://doi.org/10.1007/s10661-014-3632-
x](https://doi.org/10.1007/s10661-014-3632-
454 x), 2014.
- 455 Lagmiri, S. and Dahech, S.: Temperature Inversion and Particulate Matter Concentration in the Low Troposphere of Cergy-
456 Pontoise (Parisian Region), *Atmosphere*, 15, 349, <https://doi.org/10.3390/atmos15030349>, 2024.
- 457 Largeron, Y. and Staquet, C.: Persistent inversion dynamics and wintertime PM₁₀ air pollution in Alpine valleys, *Atmospheric
458 Environment*, 135, 92–108, <https://doi.org/10.1016/j.atmosenv.2016.03.045>, 2016.
- 459 Li, J., Chen, H., Li, Z., Wang, P., Fan, X., He, W., and Zhang, J.: Analysis of Low-level Temperature Inversions and Their

- 460 Effects on Aerosols in the Lower Atmosphere, *Adv. Atmos. Sci.*, 36, 1235–1250, <https://doi.org/10.1007/s00376-019-9018-9>,
461 2019.
- 462 Li, Y., Yan, J., and Sui, X.: Tropospheric temperature inversion over central China, *Atmospheric Research*, 116, 105–115,
463 <https://doi.org/10.1016/j.atmosres.2012.03.009>, 2012.
- 464 Liang, C., Zang, Z., Li, Z., and Yan, X.: An Improved Global Land Anthropogenic Aerosol Product Based on Satellite
465 Retrievals From 2008 to 2016, *IEEE Geosci. Remote Sensing Lett.*, 18, 944–948, <https://doi.org/10.1109/LGRS.2020.2991730>,
466 2021.
- 467 Liu, B., Ma, X., Ma, Y., Li, H., Jin, S., Fan, R., and Gong, W.: The relationship between atmospheric boundary layer and
468 temperature inversion layer and their aerosol capture capabilities, *Atmospheric Research*, 271, 106121,
469 <https://doi.org/10.1016/j.atmosres.2022.106121>, 2022.
- 470 Luo, N., Zhang, Y., Jiang, Y., Zuo, C., Chen, J., Zhao, W., Shi, W., and Yan, X.: Unveiling global land fine- and coarse-mode
471 aerosol dynamics from 2005 to 2020 using enhanced satellite-based monthly inversion data, *Environmental Pollution*,
472 <https://doi.org/10.1016/j.envpol.2024.123838>, 2024.
- 473 Ma, Y., Yao, W., and Huang, B.: Comparison of temperature and geopotential height records between 59 type and L-band
474 radiosonde systems, *Journal of Applied Meteorological Science*, 21, 214–220, <https://doi.org/10.3969/j.issn.1001-7313.2010.02.011>, 2010.
- 476 Meng, X., Wei, Z., and Ye, C.: Variation Characteristics of Ambient Air Quality in China during 2013–2022, *Environmental
477 Monitoring and Forewarning*, 15, 1–7, <https://doi.org/10.3969/j.issn.1674-6732.02023.05.001>, 2023.
- 478 Miao, Y., Che, H., Zhang, X., and Liu, S.: Integrated impacts of synoptic forcing and aerosol radiative effect on boundary layer
479 and pollution in the Beijing–Tianjin–Hebei region, China, *Atmospheric Chemistry and Physics*, 20, 5899–5909,
480 <https://doi.org/10.5194/acp-20-5899-2020>, 2020.
- 481 Milionis, A. E. and Davies, T. D.: A five-year climatology of elevated inversions at Hemsby (UK), *Intl Journal of Climatology*,
482 12, 205–215, <https://doi.org/10.1002/joc.3370120209>, 1992.
- 483 Ministry of ecology and environment the people’s republic of China: Report on the State of the Ecology and Environment in
484 China 2022, Ministry of ecology and environment the people’s republic of China, 72 pp., 2022.
- 485 Morawska, L., Zhu, T., Liu, N., Amouei Torkmahalleh, M., De Fatima Andrade, M., Barratt, B., Broomandi, P., Buonanno, G.,
486 Carlos Belalcazar Ceron, L., Chen, J., Cheng, Y., Evans, G., Gavidia, M., Guo, H., Hanigan, I., Hu, M., Jeong, C. H., Kelly,
487 F., Gallardo, L., Kumar, P., Lyu, X., Mullins, B. J., Nordstrøm, C., Pereira, G., Querol, X., Yezid Rojas Roa, N., Russell, A.,
488 Thompson, H., Wang, H., Wang, L., Wang, T., Wierzbicka, A., Xue, T., and Ye, C.: The state of science on severe air pollution
489 episodes: Quantitative and qualitative analysis, *Environment International*, 156, 106732,
490 <https://doi.org/10.1016/j.envint.2021.106732>, 2021.
- 491 Palarz, A., Celiński-Mysław, D., and Ustrnul, Z.: Temporal and spatial variability of surface-based inversions over Europe
492 based on ERA -Interim reanalysis, *Intl Journal of Climatology*, 38, 158–168, <https://doi.org/10.1002/joc.5167>, 2018.
- 493 Peng, Y., Zhao, Y., Gao, N., Sheng, D., Tang, S., Zheng, S., and Wang, M.: Spatiotemporal evolution of PM_{2.5} and its
494 components and drivers in China, 2000–2023: effects of air pollution prevention and control actions in China, *Environmental
495 Geochemistry and Health*, 47, 69, <https://doi.org/10.1007/s10653-025-02375-2>, 2025.
- 496 Rendón, A. M., Salazar, J. F., Palacio, C. A., and Wirth, V.: Temperature Inversion Breakup with Impacts on Air Quality in

497 Urban Valleys Influenced by Topographic Shading, *Journal of Applied Meteorology and Climatology*, 54, 302–321,
498 <https://doi.org/10.1175/JAMC-D-14-0111.1>, 2015.

499 Rentschler, J. and Leonova, N.: Global air pollution exposure and poverty, *Nat Commun*, 14, 4432,
500 <https://doi.org/10.1038/s41467-023-39797-4>, 2023.

501 Schiemann, Luethi, and Schaer: Seasonality and Interannual Variability of the Westerly Jet in the Tibetan Plateau Region,
502 *Journal of climate*, 22, 2009.

503 Serreze, M., Kahl, J., and Schnell, R.: Low-Level Temperature Inversions of the Eurasian Arctic and Comparisons with Soviet
504 Drifting Station Data, *Journal of Climate*, 5, 615–629, [https://doi.org/10.1175/1520-0442\(1992\)005%3C0615:LLTIOT%3E2.0.CO;2](https://doi.org/10.1175/1520-0442(1992)005%3C0615:LLTIOT%3E2.0.CO;2), 1992.

506 Shao, M., Xu, X., Lu, Y., and Dai, Q.: Spatio-temporally differentiated impacts of temperature inversion on surface PM_{2.5} in
507 eastern China, *Science of The Total Environment*, 855, 158785, <https://doi.org/10.1016/j.scitotenv.2022.158785>, 2023.

508 Stull, R. B.: *An Introduction to Boundary Layer Meteorology*, , 0, 1988.

509 Sun, M., Xie, Z., Yao, X., Wang, S., and Dong, L.: Multilayer temperature inversion structures and their potential impact on
510 atmospheric pollution in northwest China, *Atmospheric Environment*, 343, 120998,
511 <https://doi.org/10.1016/j.atmosenv.2024.120998>, 2025.

512 Vihma, T., Kilpeläinen, T., Manninen, M., Sjöblom, A., Jakobson, E., Palo, T., Jaagus, J., and Maturilli, M.: Characteristics of
513 Temperature and Humidity Inversions and Low-Level Jets over Svalbard Fjords in Spring, *Advances in Meteorology*, 2011,
514 1–14, <https://doi.org/10.1155/2011/486807>, 2011.

515 Wallace, J. and Kanaroglou, P.: The effect of temperature inversions on ground-level nitrogen dioxide (NO₂) and fine
516 particulate matter (PM_{2.5}) using temperature profiles from the Atmospheric Infrared Sounder (AIRS), *Science of The Total
517 Environment*, 407, 5085–5095, <https://doi.org/10.1016/j.scitotenv.2009.05.050>, 2009.

518 WHO: WHO global air quality guidelines: particulate matter (PM_{2.5} and PM₁₀), ozone, nitrogen dioxide, sulfur dioxide and
519 carbon monoxide, 2021.

520 Wolf, T., Esau, I., and Reuder, J.: Analysis of the vertical temperature structure in the Bergen valley, Norway, and its connection
521 to pollution episodes, *J. Geophys. Res. Atmos.*, 119, <https://doi.org/10.1002/2014JD022085>, 2014.

522 Wu, W., Zha, Y., Zhang, J., Gao, J., and He, J.: A temperature inversion-induced air pollution process as analyzed from Mie
523 LiDAR data, *Science of The Total Environment*, 479–480, 102–108, <https://doi.org/10.1016/j.scitotenv.2014.01.112>, 2014.

524 Xu, T., Song, Y., Liu, M., Cai, X., Zhang, H., Guo, J., and Zhu, T.: Temperature inversions in severe polluted days derived
525 from radiosonde data in North China from 2011 to 2016, *Science of The Total Environment*, 647, 1011–1020,
526 <https://doi.org/10.1016/j.scitotenv.2018.08.088>, 2019.

527 Xu, T., Liu, B., Zhang, M., Song, Y., Kang, L., Wang, T., Liu, M., Cai, X., Zhang, H., and Zhu, T.: Temperature inversions in
528 China derived from sounding data from 1976 to 2015, *Tellus B: Chemical and Physical Meteorology*, 73, 1898906,
529 <https://doi.org/10.1080/16000889.2021.1898906>, 2021.

530 Yan, X., Liang, C., Jiang, Y., Luo, N., Zang, Z., and Li, Z.: A Deep Learning Approach to Improve the Retrieval of Temperature
531 and Humidity Profiles From a Ground-Based Microwave Radiometer, *IEEE Trans. Geosci. Remote Sensing*, 58, 8427–8437,
532 <https://doi.org/10.1109/TGRS.2020.2987896>, 2020.

533 Yan, X., Zang, Z., Jiang, Y., Shi, W., Guo, Y., Li, D., Zhao, C., and Husi, L.: A Spatial-Temporal Interpretable Deep Learning
534 Model for improving interpretability and predictive accuracy of satellite-based PM_{2.5}, *Environmental Pollution*, 273, 116459,
535 <https://doi.org/10.1016/j.envpol.2021.116459>, 2021.

536 Yan, X., Zuo, C., Li, Z., Chen, H. W., Jiang, Y., He, B., Liu, H., Chen, J., and Shi, W.: Cooperative simultaneous inversion of
537 satellite-based real-time PM_{2.5} and ozone levels using an improved deep learning model with attention mechanism,
538 *Environmental Pollution*, 327, 121509, <https://doi.org/10.1016/j.envpol.2023.121509>, 2023.

539 Yang, J. and Shao, M.: Impacts of Extreme Air Pollution Meteorology on Air Quality in China, *JGR Atmospheres*, 126,
540 e2020JD033210, <https://doi.org/10.1029/2020JD033210>, 2021.

541 Yang, Y., Li, Z., Guo, J., Wang, Y., Wu, H., Shang, Y., Wang, Y., Zhu, L., and Yan, X.: Revolutionizing Clear-Sky Humidity
542 Profile Retrieval with Multi-Angle-Aware Networks for Ground-Based Microwave Radiometers, *J Remote Sens*, 5, 0736,
543 <https://doi.org/10.34133/remotesensing.0736>, 2025.

544 Yin, P.-Y., Chang, R.-I., Day, R.-F., Lin, Y.-C., and Hu, C.-Y.: Improving PM_{2.5} Concentration Forecast with the Identification
545 of Temperature Inversion, *Applied Sciences*, 12, 71, <https://doi.org/10.3390/app12010071>, 2021.

546 Yu, C., Zhao, T., Bai, Y., Zhang, L., Kong, S., Yu, X., He, J., Cui, C., Yang, J., You, Y., Ma, G., Wu, M., and Chang, J.: Heavy
547 air pollution with a unique “non-stagnant” atmospheric boundary layer in the Yangtze River middle basin aggravated by
548 regional transport of PM_{2.5} over China, *Atmospheric Chemistry and Physics*, 20, 7217–7230, <https://doi.org/10.5194/acp-20-7217-2020>, 2020.

550 Zang, Z., Wang, W., You, W., Li, Y., Ye, F., and Wang, C.: Estimating ground-level PM_{2.5} concentrations in Beijing, China
551 using aerosol optical depth and parameters of the temperature inversion layer, *Science of The Total Environment*, 575, 1219–
552 1227, <https://doi.org/10.1016/j.scitotenv.2016.09.186>, 2017.

553 Zang, Z., Li, D., Guo, Y., Shi, W., and Yan, X.: Superior PM_{2.5} Estimation by Integrating Aerosol Fine Mode Data from the
554 Himawari-8 Satellite in Deep and Classical Machine Learning Models, *Science of The Total Environment*, 13, 2775,
555 <https://doi.org/10.3390/rs13142779>, 2021.

556 Zhang, J., Zheng, Y., Li, Z., Xia, X., and Chen, H.: A 17-year climatology of temperature inversions above clouds over the
557 ARM SGP site: The roles of cloud radiative effects, *Atmospheric Research*, 237, 104810,
558 <https://doi.org/10.1016/j.atmosres.2019.104810>, 2020.

559 Zhang, Y. H., Zhang, S. D., Yi, F., and Chen, Z. Y.: Statistics of lower tropospheric inversions over the continental United
560 States, *Ann. Geophys.*, 29, 401–410, <https://doi.org/10.5194/angeo-29-401-2011>, 2011.

561 Zhong, J., Zhang, X., Wang, Y., Sun, J., Zhang, Y., Wang, J., Tan, K., Shen, X., Che, H., Zhang, L., Zhang, Z., Qi, X., Zhao,
562 H., Ren, S., and Li, Y.: Relative contributions of boundary-layer meteorological factors to the explosive growth of PM_{2.5}
563 during the red-alert heavy pollution episodes in Beijing in December 2016, *J Meteorol Res*, 31, 809–819,
564 <https://doi.org/10.1007/s13351-017-7088-0>, 2017.

565 Zhong, J., Zhang, X., Dong, Y., Wang, Y., Liu, C., Wang, J., Zhang, Y., and Che, H.: Feedback effects of boundary-layer
566 meteorological factors on cumulative explosive growth of PM_{2.5} during winter heavy pollution episodes in Beijing from 2013
567 to 2016, *Atmos. Chem. Phys.*, 18, 247–258, <https://doi.org/10.5194/acp-18-247-2018>, 2018.

568 Zou, J., Chen, H. W., Li, H., Wang, Q., Wang, G., Jia, K., Chen, Z., Zhao, C., Shi, W., Yang, Y., Tang, Y., Chen, J., Zhang, Y.,
569 Xu, T., Wang, Y., Liu, G., and Yan, X.: Amplified urban heat island effect in southern china’s old towns following atmospheric
570 regulation policies, *Sustainable Cities and Society*, 131, 106675, <https://doi.org/10.1016/j.scs.2025.106675>, 2025.

571 Zuo, C., Chen, J., Zhang, Y., Jiang, Y., Liu, M., Liu, H., Zhao, W., and Yan, X.: Evaluation of four meteorological reanalysis
572 datasets for satellite-based PM_{2.5} retrieval over China, *Atmospheric Environment*, 305, 119795,
573 <https://doi.org/10.1016/j.atmosenv.2023.119795>, 2023.

574